Title: Y chromosome linked UTY modulates sex differences in valvular fibroblast methylation in response to nanoscale extracellular matrix cues

Short title: UTY alters methylation states in male valve cells

Authors: Rayyan M. Gorashi[1,2], Talia Baddour[1,2], Sarah J. Chittle[1,2], Nicole E. Félix Vélez[1,2], Michaela A. Wenning[3,4], Kristi S. Anseth[5,6], Luisa Mestroni[7,8], Brisa Peña[7,8,9], Peng Guo[10], and Brian A. Aguado[1,2]*

Affiliations:

[1] Shu Chien-Gene Lay Department of Bioengineering, University of California San Diego, La Jolla, CA 92093, USA.

[2] Sanford Consortium for Regenerative Medicine, La Jolla, CA 92037, USA.

[3] Department of Chemical Engineering, Massachusetts Institute of Technology, Cambridge, MA 02139, USA.

[4] Harvard-MIT Program in Health Sciences and Technology, Massachusetts Institute of Technology, Cambridge, MA 02139, USA.

[5] Department of Chemical and Biological Engineering, University of Colorado Boulder, CO 80303, USA.

[6] BioFrontiers Institute, University of Colorado Boulder, CO 80309, USA.

[7] Cardiovascular Institute, University of Colorado Denver Anschutz Medical Campus, School of Medicine, Division of Cardiology, at 12700 E.19th Avenue, Bldg. P15, Aurora, Colorado, 80045, United States.

[8] Department of Medicine, Division of Cardiology, University of Colorado Anschutz Medical Campus, at 12700 E.19th Avenue, Bldg. P15, Aurora, Colorado, 80045, United States.

[9] Bioengineering Department, University of Colorado Denver Anschutz Medical Campus, at Bioscience 2 1270 E. Montview Avenue, Suite 100, Aurora, Colorado, 80045, United States.

[10] Nikon Imaging Center, Department of Cellular and Molecular Medicine, University of California San Diego, La Jolla, CA 92093, USA.

*Correspondence to Brian A. Aguado, PhD. Email: baguado@ucsd.edu.

Abstract

Aortic valve stenosis (AVS) is a progressive disease wherein males develop valve calcification relative to females that develop valve fibrosis. Valvular interstitial cells (VICs) aberrantly activate to myofibroblasts during AVS, driving the fibrotic valve phenotype in females. Myofibroblasts further differentiate into osteoblast-like cells and secrete calcium nanoparticles, driving valve calcification in males. We hypothesized the lysine demethylase UTY (ubiquitously transcribed tetratricopeptide repeat containing, Y-linked) decreases methylation uniquely in response to nanoparticle cues in the valve extracellular matrix to promote an osteoblast-like phenotype. Here, we describe a bioinspired hydrogel cell culture platform to interrogate how nanoscale cues modulate sex-specific methylation states in VICs activating to myofibroblasts and osteoblast-like cells. We found UTY (ubiquitously transcribed tetratricopeptide repeat containing, Y-linked) modulates VIC phenotypes in response to nanoscale cues uniquely in males. Overall, we reveal a novel role of UTY in the regulation of calcification processes in males during AVS progression.

Introduction

Aortic valve stenosis (AVS) is sexually dimorphic disease where aortic valve tissue progressively undergoes fibro-calcification[1]. AVS impacts approximately 13% of the population aged over 75, and gender-based disparities exist with clinical management of AVS, given retrospective studies suggesting women are under recommended for valve replacements. Given that valve replacement patients are also at risk for increased co-morbidities after the procedure, a significant need exists to identify non-surgical based strategies to delay the onset of AVS[2]. Clinical research further suggests the degree of fibro-calcification in the valve depends on biological sex, where males exhibit increased calcification relative to females[3,4]. Given the sex dimorphisms observed in valve tissue during AVS onset, biological sex must be considered when identifying paths toward non-surgical pharmacologic treatments for AVS.

Our collective understanding of the sex-specific fibro-calcification processes in valve tissue during AVS remain limited. Valvular interstitial cells (VICs) are the resident fibroblast-like cells in valve tissue that are known to regulate valve fibro-calcification[3]. In early stages of AVS, VICs chronically activate to myofibroblasts and express alpha smooth muscle actin (aSMA) stress fibers[5]. In moderate to late stages of AVS, myofibroblasts further differentiate into osteoblast-like valve cells[6,7]. Osteoblast-like valve cells are characterized by the nuclear localization of runt-related transcription factor (RUNX2) and contribute to the accumulation of stiff, spherical calcium phosphate nanoparticles in valve tissue[8,9]. Over time, nanoparticles increase in size and abundance and further exacerbate valve fibro-calcification[3]. We posit the initiation of sex specific AVS progression likely depends on VIC interactions with the valve extracellular microenvironment.

Calcific lesions observed in healthy and late stage AVS tissue contain dense, mineralized spherical nanoparticles (NPs) of varying size in the valve extracellular microenvironment[10]. Prior

92 studies have shown that osteoblast-like cells experience altered cytoskeletal dynamics after culture
93 on substrates containing stiff NPs[11]. In particular, the NPs affected actin organization, disrupted
94 microtubule networks, and reduced overall cell spreading. VICs interact with their surrounding
95 microenvironment via transmembrane integrin receptors[12,13]. Integrins are directly linked to the
96 actin cytoskeleton and mediate cell response to external stimuli through alterations to the nuclear
97 chromatin structure[14–16]. Prior studies have also identified differences in chromatin structure of
98 VICs from both healthy and diseased patients[17,18]. As such, chromatin re-arrangement in male and
99 female VICs in response to nanoscale cues in the extracellular matrix is hypothesized to modulate
100 sex-specific cellular phenotypes during valve fibro-calcification.

101 Furthermore, cellular responses to the extracellular microenvironment also depend on
102 intracellular sex chromosome effects[19–22]. Sex differences in AVS progression have been attributed
103 to both patient-specific sex hormone levels and sex chromosome activity[23–25]. To detangle the
104 effects of sex hormones from sex chromosome activity, approaches using hydrogel biomaterials to
105 recapitulate the valve extracellular matrix have been used to show female VICs have increased
106 myofibroblast activation due to genes that escape X chromosome inactivation[26,27]. Outside of
107 VICs, previous work has also shown hydrogels to be critical tools to understand sex-specific
108 mechanotransduction in endothelial cells cultured *in vitro*[28,29]. Our understanding of how VICs
109 respond to nanoscale cues in the extracellular matrix will continue to harness *in vitro* culture tools
110 to probe sex-specific cell-nanomaterial interactions and subsequent sex-specific effects on cell
111 phenotypes.

112 Here, we engineered a bioinspired hydrogel cell culture platform to interrogate how
113 nanoscale stiffness cues modulate the VIC-to-myofibroblast-to-osteoblast transition in males and
114 females. Hydrogel biomaterials have been used previously to culture primary VICs isolated from

115 aortic valve leaflets as a strategy to determine how sex chromosome linked genes modulate sex
116 differences in VICs phenotypes[26,27]. In our approach, we incorporated stiff, polystyrene
117 nanoparticles (PSNPs) into a water-swollen crosslinked poly(ethylene glycol) (PEG) norbornene
118 hydrogel. After culture on our PSNP hydrogel, our results collectively show male-specific
119 responses to nanoscale stiffness cues through Y-chromosome linked histone demethylase,
120 Ubiquitously Transcribed Tetratricopeptide Repeat Containing, Y-linked, UTY. After UTY
121 demethylase knockdown, we show increased methylation as well as upregulation of Transforming
122 Growth Factor Beta Receptor 1 (TGFBR1), a key promoter of calcification processes in VICs.
123 Overall, we have potentiated a role of the Y-linked UTY lysine demethylase in causing sex-specific
124 effects that guide male VICs towards calcification.
125
126 **Results**
127 **Hydrogels containing polystyrene nanoparticles mimic the valve microenvironment.**
128 We engineered a polystyrene nanoparticle (PS-NPs) hydrogel that recapitulates the valve
129 matrix that contains nano-scale calcium phosphate particles. We obtained age-matched male and
130 female aortic valve tissue (UCSD IRB 804209) from two healthy patients and two patients
131 diagnosed with AVS. Using scanning electron microscopy (SEM), we visualized the accumulation
132 of nano-scale calcium phosphate particles in aortic valve tissue from male and female AVS patients
133 relative to healthy patients (Figure 1A). After quantifying particle diameter, we observe
134 significantly larger particle sizes in males relative to females (Supplementary Figure 1). To capture
135 the range of observed particle sizes in the tissue microenvironment, we incorporated 200 or 2000
136 nm diameter PS-NPs into our polyethylene(glycol) norbornene (PEG-Nb) hydrogel network to
137 create a matrix containing nano-scale particles (Figure 1B). We quantified bulk stiffness using

138 shear rheology (Figure 1C, 1D) and surface stiffness using atomic force microscopy
139 (Supplementary Figure 2). We determined that the elastic modulus (E) of our soft, blank hydrogel
140 matrix formulation (E = 2.48 ± 0.05 kPa) does not significantly change with the incorporation of
141 200 nm PS-NPs ($E_{200\ nm\ PS\text{-}NPs,\ low}$ = 2.37 ± 0.12 kPa and $E_{200\ nm\ PS\text{-}NPs,\ high}$ = 2.98 ± 0.19 kPa) and
142 2000 nm PS-NPs ($E_{2000\ nm\ PS\text{-}NPs,\ low}$ = 3.36 ± 0.09 kPa and $E_{2000\ nm\ PS\text{-}NPs,\ high}$ = 2.55 ± 0.02 kPa),
143 relative to our stiff hydrogel formulation (E = 21.80 ± 0.36 kPa). We also utilized SEM to confirm
144 PS-NP presence on the surface of the hydrogel matrix (Figure 1E).
145
146 **Sex-specific myofibroblast activation and osteoblast-like differentiation on nanoparticle**
147 **hydrogels.**
148 To test the effect of PS-NP nanoparticles on sex-specific valve cell phenotypes, we isolated
149 valvular interstitial cells (VICs) from porcine aortic valve tissue for culture on our PS-NP
150 hydrogels (Figure 2A). First, using alpha smooth muscle actin (αSMA) stress fibers as a marker
151 of myofibroblast activation, we observed female VICs having significantly higher levels of
152 myofibroblast activation on the control, blank hydrogel without particles and PS-NP hydrogel
153 conditions, compared to male VICs (Figures 2B, 2C). Second, we evaluated the nuclear
154 localization of the transcription factor runt-related transcription factor 2 (RUNX2) as a marker of
155 osteoblast-like differentiation. Male VICs displayed significantly higher levels of RUNX2 nuclear
156 localization on the control hydrogel and most PS-NP hydrogel conditions, compared to female
157 VICs (Figures 2D, 2E). Notably, we did not observe dose-dependent or PS-NP size-dependent
158 trends in the phenotypes. Collectively, our results provide evidence that male and female VICs
159 exhibit sex-specific differences in myofibroblast and osteoblast-like phenotypes in response to PS-
160 NPs in culture. Though we detected sex-specific myofibroblast and osteoblast-like VIC

161 phenotypes in response to PS-NP hydrogels, we did not observe consistent dose-dependent or PS-
162 NP size-dependent trends in the phenotypes.
163
164 **Sex-specific methylation and acetylation states on PS-NP hydrogels.**
165 Recognizing that epigenetic modifications drive cellular phenotype plasticity via
166 alterations to methylation and acetylation states in the nucleus, we sought to characterize sex-
167 specific epigenetic states in VICs on our PS-NP gels (Figure 3A). First, to understand potential
168 cell-matrix interactions that modulate transcriptional activity, we sought to investigate methylation
169 states in VICs cultured on PS-NP hydrogels. Male VICs displayed reduced tri-methylation across
170 most hydrogel conditions relative to female VICs (Figure 3B, 3C). Interestingly, we did observe
171 dose-dependent and PS-NP size-dependent changes in methylation after culture on PS-NP
172 hydrogels. Next, we determined acetylation states in VICs cultured on PS-NP gels, with the
173 hypothesis that male VICs would have increased acetylation to drive expression of osteoblast-
174 associated genes. Interestingly, we did observe a unique trend in the males, where only larger
175 particles affected the acetylation state (Figure 3D, 3E). Male VICs also displayed significantly
176 higher acetylation states (Figure 3D) in most of our blank and PS-NP hydrogel conditions, when
177 compared to female VICs (Figure 3E). Our evidence suggests that male-specific epigenetic
178 modifications may regulate male-specific osteoblast-like differentiation on PS-NP hydrogels.
179
180 **UTY modulates male-specific methylation on PS-NP hydrogels.**
181 To investigate how epigenetic alterations regulate male-specific osteoblast-like phenotypes
182 on PS-NP hydrogels, we next hypothesized epigenetic modifiers coded on the Y-chromosome may
183 contribute to male-specific phenotypes. Specifically, we posit that a Y-linked demethylase may

184 play a key role in regulating VIC response to nanoscale cues in the extracellular matrix. We
185 interrogated the role of the Y-linked global demethylase Ubiquitously Transcribed
186 Tetratricopeptide Repeat Containing, Y-linked (UTY) in regulating VIC phenotype and variable
187 methylation on PS-NP hydrogels. We first validated the male-specific mRNA expression of *UTY*
188 using real time quantitative polymerase chain reaction (RT-qPCR) (Figure 4A). Next, we employed
189 a small interfering RNA (siRNA) targeting the *UTY* gene to transcriptionally silence *UTY* while
190 VICs are cultured on PS-NP hydrogels. We utilized RT-qPCR to validate that we significantly
191 reduced relative *UTY* gene expression compared to our Silencer control uniquely in male VICs
192 (Figure 4B). Female VICs did not show significant *UTY* expression in all our conditions, further
193 validating a male-specific reduction in *UTY* expression. As another means of validation, we next
194 used immunofluorescence to detect global methylation in male and female VIC nuclei (Figure 4C).
195 As hypothesized, UTY knockdown in male VICs lead to a significant increase in methylation on
196 blank hydrogels (Figure 4D). Interestingly, UTY knockdown in female VICs also increased
197 methylation on blank gels, although the effect was more pronounced in male VICs. On PS-NP
198 gels, UTY knockdown did not impact methylation in male or female VICs. Together, we suggest
199 UTY modulates male-specific methylation states in VICs cultured on our engineered hydrogels.
200

201 **Bulk sequencing and gene ontology unveils upregulation of pro-osteogenic differentiation**
202 **pathways after *UTY* siRNA.**

203 Given the sex-specific differences in myofibroblast and osteoblast-like phenotypes, in
204 addition to sex-specific methylation and acetylation states, we performed bulk mRNA sequencing
205 to understand the sex-specific transcriptomic responses to *UTY* siRNA treatment. In both blank
206 and PS-NP gels, male VICs displayed a larger number of differentially expressed genes (DEGs)

207 compared to female VICs (Figure 5A-B, Supplemental Figure 3A-3B). Gene ontology (GO)
208 enrichment analysis of male VICs with *UTY* knockdown reveal upregulated DEGs associated with
209 organelle assembly, cell morphogenesis, responses to mechanical stimulus, cilium organization,
210 and Transforming Growth Factor Beta Receptor (TGFBR) signaling, among others (Figure 5C).
211 After *UTY* knockdown, downregulated DEGs in male VICs associated with GO terms including
212 GTP binding, guanyl ribonucleotide binding, and protein kinase binding (Figure 5D). In females,
213 many upregulated and downregulated DEGs after siRNA treatment were associated with pathways
214 involving cell metabolism and cell cycle regulations (Supplemental Figure 3C-3D). We speculate
215 that these pathways were differentially expressed because of the internalization of the siRNA
216 delivery vehicle, rather than the presence of the *UTY* siRNA itself. Collectively, our RNAseq
217 data suggest *UTY* modulates pathway activity uniquely in male VICs responding to PS-NP gels.
218

219 **Discussion**

220 Here, we highlight that the Y-chromosome modulates male-specific VIC phenotypes to
221 nanoscale cues in the extracellular matrix relative to female VICs (Figure 6). Using PEG hydrogels
222 with polystyrene nanoparticles as a platform for cell culture, we show the protein-coding gene
223 *UTY* may modulate male-specific demethylation in VICs during calcification in AVS. Recent
224 studies have described the significant role of the mosaic loss of the Y-chromosome (mLOY) in
225 male-specific cardiovascular disease progression[30,31,32]. mLOY occurs as an aging-related
226 mutation in males, though the heterogeneity in mLOY in varying cell types and relation disease
227 progression is not well understood. In the context of AVS, significant positive associations between
228 transcatheter aortic valve replacement (TAVR) patient mortality and presence of mLOY in
229 circulating monocytes have been reported[30]. Transcriptomic studies on mLOY monocytes revealed

230 a profibrotic gene signature, suggesting their role in driving restenosis post-TAVR. Furthermore,
231 *UTY* is also known to protect against proinflammatory phenotypes in lung tissue during pulmonary
232 hypertension. Specifically, *UTY* knockdown resulted in significant increases in the production of
233 proinflammatory cytokines CXCL9 and CXCL10, recruiting macrophages and promoting a
234 fibrotic phenotype in the lung tissue[33]. Our results here further corroborate prior efforts implicating
235 Y chromosome linked genes, including *UTY*, as key male-specific modulators of male-specific cell
236 phenotypes[33,30,31]. Together, our work here provides a hydrogel cell culture platform that enables
237 the interrogation of Y chromosome linked genes and their impact on male-specific cellular
238 phenotypes.

239 To the best of our knowledge, our study is the first to directly show *UTY* influences male-
240 specific VIC myofibroblast activation and osteoblast-like differentiation in response to
241 extracellular mechanical cues. Primary VICs from porcine sources have long been utilized to
242 evaluate myofibroblast activation and osteogenic differentiation processes in AVS in response to
243 different bulk substrate stiffnesses[28,34–39]. For example, in response to tissue culture plastic (elastic
244 modulus, E ~ 1 GPa), VICs automatically activate to myofibroblasts through the expression of α-
245 SMA stress fibers[26]. As an alternative approach, hydrogel biomaterial platforms composed of PEG
246 and a variety of crosslinking chemistries have been used to study VIC mechanosensitivity and sex-
247 specific modulation of myofibroblast activation and osteoblast differentiation states. For example,
248 previous work has shown that VICs cultured in 2D or 3D PEG-norbornene hydrogels in the ~1
249 kPa to ~40 kPa stiffness regime recapitulates sex-specific myofibroblast phenotypes observed in
250 valve tissue[26,27]. PEG hydrogel cell culture platforms also showed X chromosome inactivation
251 genes and the p38 MAPK signaling pathway partially regulate female-specific myofibroblast
252 activation processes[27]. Using a similar hydrogel system, we implemented a bio-inspired approach

253 where we incorporated nanoparticles into the hydrogel matrix to mimic nanoscale features in valve
254 tissue, as apparent in our SEM images and previous work. Inflammatory cytokines were found to
255 direct myofibroblasts towards the osteogenic pathway toward calcification[40]. Our work suggests
256 that nuclear localization of runt-related transcription factor 2 (RUNX2) in VICs responding to
257 nanoscale features in tissue may modulate a male-specific bias toward the initiation of calcification
258 processes. One of the most upregulated GO terms in males after *UTY* siRNA on PS-NP hydrogels
259 included Transforming Growth Factor Beta Receptor (TGFBR) signaling. Prior studies have
260 identified TGFBR1 as a key mediator in myofibroblast and osteogenic differentiation processes,
261 indicating a potential role for *UTY* in regulating pathways associated with fibro-calcification[41–43].
262 Enabled with our hydrogel platform, our work provides evidence for a novel mechanism
263 describing UTY as a candidate regulator of myofibroblast and osteoblast-like phenotypes in male
264 VICs, furthering our knowledge on how sex chromosomes may broadly contribute to somatic cell
265 phenotypes.

266 Our study also showcased the role of *UTY* in modulating the global transcriptional
267 landscape in VICs responding to hydrogel microenvironments via modulations in tri-methylation
268 and acetylation markers. Many studies have linked activity of mechanosensitive cell surface
269 receptors in modulating epigenetic states in the nucleus[17,18]. Epigenetic modifications can occur in
270 response to an external mechanical stimulus, which alters the conformation of the cell's surface
271 receptor, altering the structure of the connected intracellular cytoskeletal network tied to the
272 nucleus[22]. Diseased myofibroblasts have also been shown to maintain distinct chromatin structures
273 in response to bulk stiffness cues in PEG-acrylate gels, compared to healthy myofibroblasts. The
274 altered mechanical tension on the nucleus influences epigenetic processes that can transcriptionally
275 activate (acetylation) or silence (methylation) different regions of chromatin. A prior study using

276 VICs showed that stiff hydrogels promoted increased acetylation in male VICs compared to soft
277 hydrogels, however, the specific epigenetic alterations and the mechanisms by which they occur
278 are still poorly understood. Building upon this work, we show that male specific methylation and
279 acetylation states may be modulated via *UTY* demethylase activity. Prior studies have investigated
280 various phenotypic changes of VICs in response to a variety of mechanical cues. When evaluating
281 methylation in males, we observed a consistent trend in decreased methylation correlating with
282 particle size and density, indicating male myofibroblasts uniquely interact with nanoscale features
283 in an extracellular microenvironment. Interestingly, female VICs did not show a decrease in
284 methylation when interacting with nanoscale cues, but did reduce methylation with larger
285 nanoparticles, indicating other demethylases may participate in female-specific cell-particle
286 interactions. A previous study showed that female human embryonic stem cells cultured with silver
287 nanoparticles have compromised differentiation processes via disordered X chromosome
288 inactivation, although female-specific effects of nanoparticles on pluripotent vs somatic cell
289 cultures have yet to be compared[44]. Future efforts will need to assess the role of other demethylases
290 in common between XY and XX cells, or potential activity of X-linked demethylases (e.g. *UTX,*
291 *KDM5C*, etc.) to supplement our observations in male VICs.

292 There are several limitations of the PSNP hydrogel platform described in our study. First,
293 our study did not decouple the effects of sex hormones from sex chromosomes. For future work,
294 a gonadectomized animal model can probe the effects of the sex chromosome on VIC phenotype.
295 Sex hormones could also be dosed into the hydrogel platform, further interrogating the intersection
296 between sex hormone and sex chromosome effects. Secondly, our study sought to characterize the
297 VIC-nanoparticle interactions on a soft hydrogel matrix. In the diseased AV environment, VICs
298 interact with a variety of mechanical and biochemical cues. Our study did not include biochemical

factors such as secreted inflammatory cytokines, which are present in the diseased AV due to immune cell infiltration. Future cell culture platforms can be adapted to include inflammatory factors secreted from macrophages to evaluate epigenetic modifications in response to inflammatory cytokines and nanoscale stiffness cues. Third, our study also evaluated cell phenotypes after two days in culture. Acknowledging that AVS is a time-dependent progressive disease, we suggest future studies where longer timepoints are used to evaluate sex-specific chromatin structures (e.g. after 7 days in culture) as VICs acquire a more permanent myofibroblast phenotype reflective of diseased valve tissue. Fourth, future efforts to use spherical calcium phosphate particles instead of PS-NPs may be used to further enhance the physiological relevance of the *in vitro* culture platform and evaluate effects of UTY and other Y-linked genes on calcification[45].

Taken together, our study implicates the importance of sex chromosome-linked genes in the progression of disease-driving phenotypes in AVS. Our bioinspired hydrogel platform provides evidence that nanoscale cues in the extracellular matrix influence sex-specific phenotypes in VICs, and broadly suggests biomaterials are useful tools to answer research questions related to sex-specific biology[46,47]. We posit that Y-linked epigenetic regulators, such as UTY, regulate male-specific osteoblast-like phenotypes, contributing to earlier onset of valvular calcification in males. Future studies will explore the interplay between mechanical stimuli and sex-specific epigenetic regulation in males and females.

322 **Materials and Methods**

323 *Nanoparticle hydrogel fabrication*

324 8-arm, 40 kDa polyethylene(glycol)-norbornene (PEG-Nb) was synthesized as previously
325 described[48]. Hydrogel precursor solutions were made mixing together 4% (w/v) PEG-Nb, 5 kDa
326 PEG-dithiol crosslinker (2.96 mM, JenKem), CRGDS peptide (2 mM, Bachem), phosphate
327 buffered saline (PBS, Gibco, 14-190-250), and photoinitiator lithium phenyl-2,4,6-trimethyl-
328 benzoylphosphinate (1.7 mM, Sigma, 900889). To incorporate nanoparticles into hydrogel
329 precursor solutions, polystyrene nanoparticle solutions, we utilized 1% wt/vol aqueous solutions
330 of 200 nm (Nanocs, PS01-200) or 2000 nm (Nanocs, PS01-2u) polystyrene nanoparticles (PS-
331 NPs) instead of PBS in the hydrogel precursor formulation. All hydrogels were made utilizing a
332 0.99:1 thiol-to-ene ratio. Vapor deposition was used to functionalize 12 mm glass coverslips
333 (Mercedes Scientific, MER0012) and 25 mm glass coverslips (Mercedes Scientific, MER0025)
334 with thiol groups to allow for hydrogel adhesion. Briefly, coverslips were placed in an autoclave
335 jar along with 100 μL of mercaptopropyltrimethoxysilane (MPTS, Sigma-Aldrich, X) in a 60°C
336 oven overnight for thiol functionalization. Glass slides were coated with Sigmacote (Sigma-
337 Aldrich, 175617) to create a hydrophobic glass surface during hydrogel fabrication. Either 11.3 μL
338 or 65 μL of hydrogel precursor solution was pipetted onto the Sigmacote glass slide and covered
339 with a 12 mm or 25 mm coverslip, respectively. The hydrogels were photopolymerized at 4
340 mW/cm^2, removed with a razor blade, sterilized with 5% isopropyl alcohol/PBS solution, and
341 rinsed three times with PBS. After the final PBS rinse, cell culture media containing Media 199
342 (Gibco, 11043023) supplemented with 1% Fetal Bovine Serum (Gibco, 16000069), and 50 units
343 penicillin, and 0.05 mg/ml streptomycin (Sigma Aldrich, P4458) was added to the hydrogels for
344 overnight swelling prior to cell culture.

Rheology

Hydrogels containing nanoparticles were prepared as described above for rheological measurements. Storage (G') and loss (G'') moduli were measured using a DHR-3 rheometer (TA Instruments) with an 8 mm parallel plate geometry. Oscillatory shear rheology was used with an amplitude of 1% and frequency of 1 Hz[26]. To obtain the elastic modulus (E), the following formula was used: E = 2 * G' (1 + v) where v is Poisson's ratio. We utilized a value of v = 0.5, assuming G' >>> G'' for viscoelastic hydrogels.

Scanning Electron Microscopy (SEM) on Hydrogels and Human Valve Tissue and quantification of particle size distribution

For scanning electron microscopy (SEM) of hydrogels, samples were prepared on coverslips, frozen in liquid nitrogen, and lyophilized. SEM was performed using a JSM-6010LA instrument (JEOL Ltd, CU Anschutz) using manufacturer settings. For SEM on human valve tissue, samples were fixed, paraffin embedded, and sectioned onto glass slides. Samples were sputter coated with iridium for 30 seconds at 75% power and imaged using a FEI Quanta FEG 250 (FEI) using manufacturer settings. Average calcium particle size was determined from two biological replicates for each sex in the disease condition using ImageJ.

Atomic Force Microscopy (AFM)

For atomic force microscopy, hydrogels mounted on coverslips were immersed in PBS and analyzed using a JPK NanoWizard 4a instrument (JPK Instruments). Hydrogels were probed using CB3 cantilevers with triangular tips (Nanosensors, qp-BioAC-CI) until an initial force of 1 nN was reached. Calibration of the cantilever was made applying the thermal noise method. Force

368 spectroscopy was performed at each node of a square grid distributed over a 20 μm by 20 μm grid.
369 Force–displacement (F–d) data were collected using a peak load of 5 nN at a displacement rate of
370 10 μm/s. Force–deformation (F–δ) data were calculated using F–d curves by subtracting the initial
371 cantilever deflection. To determine Young's modulus E at each node, the loading portion of each
372 F–δ curve was fit to an analytical model for a rigid conical tip in contact with an elastic half-space
373 (38), i.e., $F=(2/\pi)(E/1-\nu^2)(\tan\alpha)\delta^2$, using angle α determined from SEM images, an assumed
374 Poisson's ratio for the hydrogel ($\nu = 0.5$), and E as the sole fitting parameter.
375
376 *Porcine valvular interstitial cell isolation and culture*
377 Aortic valves (AVs) were dissected from 5-8-month-old male or female pigs (Midwest
378 Research Swine) to obtain valvular interstitial cells (VICs). For each isolation, four to eight porcine
379 hearts were separated by sex and pooled. Each batch of VICs obtained from an isolation is
380 considered as a biological replicate, in which 2-3 biological replicates were used for Figures 2-6.
381 After dissection, AV leaflets were submerged and rinsed in Earle's Balanced Salt Solution (EBSS,
382 Sigma Aldrich, E2888) containing 50 units penicillin and 0.05 mg/ml streptomycin. Next, leaflets
383 were digested in EBSS containing 250 units of Collagenase type 2 (Worthington Biochemical,
384 LS004176) for 30 minutes at 37°C under constant agitation at 100 rpm. After, collagenase solution
385 was aspirated from the AV leaflets to remove endothelial cells. A secondary digestion with fresh
386 collagenase solution was performed for 60 minutes under agitation at 100 rpm. To collect VICs,
387 the remaining tissue was scraped against a 100 μm cell strainer, washed with VIC media, then
388 centrifuged at 400 g for 10 minutes. The supernatant was aspirated and replaced with fresh VIC
389 expansion media, comprised of Media 199 supplemented with 15% FBS, and 50 units penicillin
390 and 0.05 mg/ml streptomycin. Freshly isolated VICs were cultured in VIC expansion media with

391 media changes every other day until confluency. VICs were frozen down at passage 1. All
392 experiments utilized passage 2 VICs at 35,000 cells/cm^2. To reduce proliferation during
393 experimentation, passage 2 VICs were cultured in VIC media containing 1% FBS.
394
395 *Small-interfering RNA (siRNA) Gene Knockdown*
396 Gene knockdowns in the porcine VICs were conducted using small interfering RNAs
397 (siRNAs). We utilized Ubiquitously Transcribed Tetratricopeptide Repeats, Y-linked (*UTY*) siRNA
398 (Ambion, 4392421 ID: s14740). On Day 0, cells were seeded at 42,000 cells/cm^2 coverslips in 1%
399 VIC media, without antibiotics or antifungal supplements, and cultured overnight. We increased
400 cell seeding density per manufacturer recommendations for siRNA experiments. On Day 1, *UTY*
401 siRNAs and Silencer negative control (Ambion, AM4635) were incubated with Lipofectamine
402 3000 Transfection Reagent (Thermo Scientific, L3000008) for 15 minutes at room temperature
403 before adding it to fresh 1% VIC media without antibiotics. The final siRNA concentration for the
404 12 mm and 25 mm hydrogels was 20 pmol and 100 pmol, respectively. On Day 2, the samples
405 were monitored without media change. On Day 3, the samples were fixed for immunofluorescence
406 and lysed for RNA collection. In total, *UTY* siRNA treatment lasted 48 hours.
407
408 *Immunofluorescence, Imaging, and Analysis*
409 Cells were cultured on NP hydrogels for 48 hours before fixing with 4% (w/v)
410 paraformaldehyde (Electron Microscopy Sciences, 15710) for 20 minutes. Afterwards, cells were
411 permeabilized with 0.1% (w/v) Triton-X-100 (Sigma Aldrich, 93443) for one hour.
412 Permeabilization buffer was removed and added 5% (w/v) bovine serum albumin (BSA, Sigma
413 Aldrich, A8327) as blocking buffer overnight at 4°C. The following primary antibodies were

414 diluted in blocking buffer and incubated for one hour at room temperature: α-smooth muscle actin
415 (aSMA, 1:300, Abcam, ab7817), runt-related transcription factor 2 (RUNX2, 1:300, Abcam,
416 ab23981), Methyl-Lysine (MeK, 1:350, Novus Biologicals, NB600824), and acetylated lysine
417 (AcK, 1:350, Abcam, ab190479). Samples were rinsed with 0.05% (v/v) Tween-20 (Sigma
418 Aldrich, P1379) for 5 minutes. The following secondary antibodies were diluted in blocking buffer
419 and incubated for one hour at room temperature protected from light: AlexaFluor 488 goat anti-
420 mouse (1:200, Thermo Scientific, A11001), AlexaFluor 647 goat anti-rabbit (1:200, Thermo
421 Scientific, A21245), or AlexaFluor 647 donkey anti-rabbit (1:200, Thermo Scientific, A32790).
422 Nuclei were stained with DAPI (1:500, Roche, 10236276001) and cytoplasm were stained with
423 CellMask Orange (1:5000, Fisher Scientific, H32713). Sample coverslips were rinsed with PBS
424 and transferred to a glass-bottom well plate (CellVis, P24-1.5H-N) for imaging on a Nikon Eclipse
425 Ti2-E. Fluorescence was quantified after modifying a freely available MATLAB code[27], and
426 fluorescence channel exposure was adjusted consistently in all conditions for representative image
427 clarity. Alpha smooth muscle actin intensity ratios were calculated by normalizing α-SMA
428 intensity with CellMask cytoplasmic intensity. Nuclear RUNX2 intensity ratios were calculated
429 by normalizing RUNX2 nuclear intensity to cytoplasmic intensity. Nuclear methylated lysine
430 ratios were calculated by normalizing MeK nuclear intensity to cytoplasmic intensity. Nuclear
431 acetylated lysine ratios were calculated by normalizing AcK nuclear intensity to DAPI intensity.
432
433 *RNA Isolation and RT-qPCR*
434 RNA was collected at specified timepoints using the RNeasy Micro Kit (Qiagen, 74004)
435 following the manufacturer's protocol. Gels on 25 mm coverslips were inverted onto lysis buffer
436 for 3 minutes then rinsed with 70% (v/v) ethanol to collect lysed cellular material. After following

437 manufacturer's protocol for RNA isolation, samples were analyzed for mRNA concentration using
438 a NanoDrop 2000 spectrophotometer (Thermo Scientific). Sample concentrations were normalized
439 to 1 ng/µL during cDNA preparation using the iScript Synthesis Kit (Bio-Rad, 1708841), following
440 manufacturer's protocol. To measure relative gene expression, iQ SYBR Green Supermix (Bio-
441 Rad, 1708882) was mixed with primer sequences found in Supplemental Table 1. Cq values were
442 determined using a CFX384 iCycler (Bio-Rad). All gene expression calculations were normalized
443 to *RPL30* expression.
444
445 *Bulk RNA Sequencing and Analysis*
446 Prior to bulk paired-end RNA sequencing, RNA was isolated as described above. RNA quality
447 was assessed by Agilent TapeStation 4200 and RNA quantity was determined by QuBit 3.0
448 Fluorometer. Approximately 200 ng of RNA per sample was used for sequencing. The Sanford
449 Consortium for Regenerative Medicine's Genomics Core conducted cDNA library preparation and
450 indexing using the Illumina Stranded mRNA kit and IDT Illumina RNA UD Indexes, respectively.
451 Sequences were checked for quality control using fastqc (v0.12.1) and subsequently removed
452 adapter sequences using trimmomatic (v0.39) if adapter sequence content exceeded the threshold
453 identified by fastqc. Alignment to the porcine genome (Sscrofa11.1) was conducted using HISAT2
454 2.2.1. Subsequent differential gene expression analysis was conducted in R (4.3.2) and R Studio
455 (2023.12.1) using DESeq2 (Release 3.19) before we filtered for genes with a false discovery rate
456 above 0.1. We utilized gene ontology analysis features in Ingenuity Pathway Analysis (Qiagen) for
457 gene enrichment analyses of upregulated and downregulated genes in the PS-NP samples.
458
459

Statistical Analysis

For immunofluorescence studies, one-way ANOVA with Tukey's posttests were conducted. We set a threshold of significance cutoff at $P < 0.0001$. Due to the experimental sample size ($N > 700$ cells), we sought to reduce statistical bias by conducting a Cohen's d-value test to determine significance independent of sample size. Thresholds of significance were represented by the following key: *** = $d > 0.8$, ** = $d > 0.5$, * = $d > 0.2$ for between sex significance; ### = $d > 0.8$, ## = $d > 0.5$, # = $d > 0.2$ for male group significance; and $$$ = $d > 0.8$, $$ = $d > 0.5$, $ = $d > 0.2$ for female group significance. For RT-qPCR studies, one-way ANOVA with Tukey's posttests were conducted. For Figure 1, data is shown as the mean ± standard deviation, as calculated in GraphPad PRISM.

Figure Captions

Figure 1. PS-NP hydrogels recapitulate nano-scale features in aortic valve tissue ECM. (A) Scanning electron microscopy (SEM) images of male healthy, diseased, and female diseased human aortic valve leaflets. Scale bar = 5 μm. (B) Schematic of process to incorporate polystyrene nanoparticles (PS-NPs) into PEG-Norbornene hydrogel precursor solutions to create PS-NP hydrogels adhered to glass coverslips via UV polymerization. (C) Rheological characterization of UV-mediated polymerization of soft, stiff, and PS-NP hydrogels made with 200 nm and 2000 nm nanoparticles (n=3 representative measurements) at low and high concentrations (0.02 mg/ml and 0.7 mg/ml, respectively). (D) Young's modulus (E) values for soft, stiff, and PS-NP hydrogels (N=3 gels). Significance determined via one-way ANOVA (****$p<0.0001$ denoting statistical significance between hydrogel formulations). Mean ± SD shown. (E) SEM of blank and PS-NP hydrogels (200 nm, 2000 nm). Yellow arrows denote PS-NPs. Scale bar = 5 μm.

Figure 2. Male and female VICs exhibit sex-specific myofibroblast and osteoblast-like phenotypes.

(A) Schematic describing experimental workflow for probing myofibroblast activation with α-smooth muscle actin (α-SMA) and osteoblast-like differentiation with runt related (RUNX2). Figure drawn with BioRender. (B) Representative confocal microscopy images of alpha smooth muscle stress fibers (green) and nuclei (blue). Scale bar = 50 μm. (C) Normalized α-SMA expression ratios for male and female VICs cultured on control hydrogels with no PS-NPs, 200 nm PS-NPs, or 2000 nm PS-NPs at low and high concentrations (0.02 mg/ml and 0.7 mg/ml, respectively). Significance determined via Cohen's d-test (*d < 0.2, **d < 0.5, ***d<0.8, ****d<1.4 denoting significance between biological sex in the provided table, red asterisk color indicates significant increase in female groups, $^{\#}$d < 0.2, $^{\#\#}$d < 0.5 denoting significance relative to male control with no particles, $^{\$\$}$d < 0.5, $^{\$\$\$}$d < 0.8 denoting significance relative to female control with no particles). (D) Representative confocal microscopy images of RUNX2 expression (red) and nuclei (blue). Scale bar = 50 μm. (E) RUNX2 nuclear to cytoplasmic intensity ratios of male and female VICs cultured on control hydrogels with no PS-NPs, 200 nm PS-NPs, or 2000 nm PS-NPs at low and high concentrations (0.02 mg/ml and 0.7 mg/ml, respectively). Significance determined via Cohen's d-test (*d < 0.2, **d < 0.5, ***d<0.8, ****d<1.4 denoting significance between biological sex in the provided table, blue asterisk color indicates significant increase in male groups, $^{\#}$d < 0.2, $^{\#\#}$d < 0.5 denoting significance relative to male control with no particles, $^{\$\$}$d < 0.5, $^{\$\$\$}$d < 0.8 denoting significance relative to female control with no particles.

Figure 3. Male and female VICs exhibit sex-specific changes in global methylation and acetylation states.

(A) Schematic describing experimental workflow for assessing sex-specific methylation and acetylation states in VICs cultured on PS-NP gels. Figure drawn with BioRender. (B) Representative confocal microscopy images of methylated lysine (yellow) and nuclei (blue). Scale bar = 50 μm. (C) Normalized nuclear intensity ratios of methylated lysine to DAPI in male and female VICs cultured on control hydrogels with no PS-NPs, 200 nm PS-NPs, or 2000 nm PS-NPs at low and high concentrations (0.02 mg/ml and 0.7 mg/ml, respectively) . Significance determined via Cohen's d-test (**d < 0.5, ***d<0.8, ****d<1.4 denoting significance between biological sex in the provided table, red asterisk color indicates significant increase in female groups, $^{\#}$d < 0.2, $^{\#\#}$d < 0.5, $^{\#\#\#}$d<0.8, $^{\#\#\#\#}$d<1.4 denoting significance relative to male control with no particles, $^{\$}$d < 0.2 denoting significance relative to female control with no particles). (D) Representative confocal microscopy images of acetylated lysine (yellow) and nuclei (blue). Scale bar = 50 μm. (E) Normalized nuclear intensity ratios of acetylated lysine to DAPI in male and female VICs cultured on control hydrogels with no PS-NPs, 200 nm PS-NPs, or 2000 nm PS-NPs at low and high concentrations (0.02 mg/ml and 0.7 mg/ml, respectively). Significance determined via Cohen's d-test (*d<0.2, **d < 0.5 denoting significance between biological sex in the provided table, blue asterisk color indicates significant increase in male groups, $^{\#}$d < 0.2, $^{\#\#\#}$d<0.8 denoting significance relative to male control with no particles, $^{\$}$d < 0.2, $^{\$\$}$d < 0.5 denoting significance relative to female control with no particles).

527 **Figure 4. Male-specific methylation is uniquely increased in male VICs by siRNA-targeting**
528 **of Y-linked demethylase, UTY.**
529 (A) Real time quantitative polymerase chain reaction (RT-qPCR) for relative expression of *UTY*
530 in male and female VICs cultured on blank, 200 nm, and 2000 nm PS-NP hydrogels. (B) RT-qPCR
531 to validate partial silencing of *UTY* in male VICs after introduction of siRNA vector. (C)
532 Representative confocal microscopy images of methyl lysine (red) and nuclei (blue). Scale bar =
533 50 μm. (D) Normalized nuclear intensity ratios of methylated lysine in male and female VICs
534 cultured on control hydrogels with no PS-NPs and 2000 nm PS-NPs. Significance determined via
535 Cohen's d-test (*d<0.2, **d < 0.5 denoting significance between biological sex in the provided
536 table, blue asterisk color indicates significant increase in male groups, $^{\#}$d < 0.2, $^{\#\#\#}$d<0.8 denoting
537 significance relative to male control with no particles, $^{\$}$d < 0.2, $^{\$\$}$d < 0.5 denoting significance
538 relative to female control with no particles).
539
540 **Figure 5. Bulk sequencing and gene ontology enrichment analysis in male VICs unveils**
541 **upregulated and downregulated GO terms.**
542 (A) Bulk mRNA sequencing shows differentially expressed genes in male VICs (blue =
543 downregulated, red = upregulated, gray = not significant) in control and PS-NP hydrogels using
544 DESeq2 (n=2 biological replicates). (B) Upregulated and (C) downregulated gene ontology-based
545 pathways that are enriched for genes differentially expressed in control and PS-NP hydrogels after
546 *UTY* siRNA treatment.
547
548
549

550 **Figure 6. Proposed mechanism revealing UTY as a candidate mediator of male-specific**
551 **demethylation.**
552 (A) Male VICs have increased nuclear localization on blank hydrogels, and nuclear localization of
553 RUNX2 increases when male VICs respond to PS-NPs embedded in the matrix. UTY reduces
554 methylation in male VICs responding to PS-NPs, and methylation is restored after UTY
555 knockdown. (B) Female VICs have increased α-SMA stress fiber formation relative to male VICs
556 on blank hydrogels, with lower nuclear localization of RUNX2 and equivalent methylation and
557 acetylation. Female VICs responding to PS-NPs have uniquely reduced α-SMA stress fiber
558 formation with increases in acetylation.
559

560 **Acknowledgements**

561 R.M.G. acknowledges support from a National Institutes of Health Research Supplement to
562 Promote Diversity in Health-Related Research (R00 HL148542) and the San Diego ARCS
563 Foundation. T.B. acknowledges support from the San Diego Match Fellowship. N.E.F.
564 acknowledges support from a National Institutes of Health Research Supplement to Promote
565 Diversity in Health-Related Research (R00 HL148542) and support from the National Science
566 Foundation Graduate Research Fellowship Program. B.P and L.M acknowledge funding from the
567 National Institutes of Health (NIH) National Heart, Lung, and Blood Institute (NHLBI): grants
568 K25HL148386 (B.P.), R01HL169578 (B.P.), and R01HL147064 (L.M.), the NIH National
569 Institute of Aging (NIA) R21AG080257 (BP), the Ludeman Family Center for Women's Health
570 Research seed grant (B.P.), the American Heart Association (AHA): 23CDA1052411 (B.P.). This
571 study was also supported by generous grants of the John Patrick Albright (L.M. and B.P.). B.A.A.
572 acknowledges support from the National Institutes of Health (R00 HL148542), the NIH Director's

New Innovator Award (DP2 HL173948), the Chan Zuckerberg Initiative Science Diversity Leadership Award, and the American Heart Association (22CDA942253). We acknowledge the help and resources of Dr. Guillaume Castillon at the Electron Microscopy Core and Dr. Zhicheng Long at the Nanofabrication core at the University of California San Diego.

596 **References**

597 1. Carabello BA, Paulus WJ. Aortic stenosis. *The Lancet*. 2009;373(9667):956-966.
598 doi:10.1016/S0140-6736(09)60211-7

599 2. Myasoedova VA, Ravani AL, Frigerio B, et al. Novel pharmacological targets for calcific
600 aortic valve disease: Prevention and treatments. *Pharmacol Res*. 2018;136:74-82.
601 doi:10.1016/j.phrs.2018.08.020

602 3. Simard L, Côté N, Dagenais F, et al. Sex-Related Discordance Between Aortic Valve
603 Calcification and Hemodynamic Severity of Aortic Stenosis. *Circ. Res.* 2017;120(4):681-691.
604 doi: 10.1161/CIRCRESAHA.116.309306.

605 4. Gourgas O, Khan K, Schwertani A, Cerruti M. Differences in mineral composition and
606 morphology between men and women in aortic valve calcification. *Acta Biomater*.
607 2020;106:342-350. doi:10.1016/j.actbio.2020.02.030

608 5. Ayoub S, Lee CH, Driesbaugh KH, et al. Regulation of valve interstitial cell homeostasis by
609 mechanical deformation: implications for heart valve disease and surgical repair. *J R Soc*
610 *Interface*. 2017;14(135):20170580. doi:10.1098/rsif.2017.0580

611 6. Goody PR, Hosen MR, Christmann D, et al. Aortic Valve Stenosis. *Arterioscler Thromb Vasc*
612 *Biol*. 2020;40(4):885-900. doi:10.1161/ATVBAHA.119.313067

613 7. Blaser MC, Kraler S, Lüscher TF, Aikawa E. Multi-Omics Approaches to Define Calcific
614 Aortic Valve Disease Pathogenesis. *Circ Res*. 2021;128(9):1371-1397.
615 doi:10.1161/CIRCRESAHA.120.317979

616 8. Nagy E, Eriksson P, Yousry M, et al. Valvular osteoclasts in calcification and aortic valve
617 stenosis severity. *Int J Cardiol*. 2013;168(3):2264-2271. doi:10.1016/j.ijcard.2013.01.207

618 9. Yu C, Li L, Xie F, et al. LncRNA TUG1 sponges miR-204-5p to promote osteoblast
619 differentiation through upregulating Runx2 in aortic valve calcification. *Cardiovasc Res*.
620 2018;114(1):168-179. doi:10.1093/cvr/cvx180

621 10. Bertazzo S, Gentleman E. Aortic valve calcification: a bone of contention. *Eur Heart J*.
622 2017;38(16):1189-1193. doi:10.1093/eurheartj/ehw071

623 11. Ibrahim M, Schoelermann J, Mustafa K, Cimpan MR. TiO2 nanoparticles disrupt cell
624 adhesion and the architecture of cytoskeletal networks of human osteoblast-like cells in a size
625 dependent manner. *J Biomed Mater Res A*. 2018;106(10):2582-2593.
626 doi:10.1002/jbm.a.36448

627 12. Chen JH, Simmons CA, Towler DA. Cell–Matrix Interactions in the Pathobiology of
628 Calcific Aortic Valve Disease. *Circ Res*. 2011;108(12):1510-1524.
629 doi:10.1161/CIRCRESAHA.110.234237

630 13. Kodigepalli KM, Thatcher K, West T, et al. Biology and Biomechanics of the Heart Valve
631 Extracellular Matrix. *J Cardiovasc Dev Dis*. 2020;7(4):57. doi:10.3390/jcdd7040057

632 14. Barczyk M, Carracedo S, Gullberg D. Integrins. *Cell Tissue Res*. 2010;339(1):269-280.
633 doi:10.1007/s00441-009-0834-6

634 15. Takada Y, Ye X, Simon S. The integrins. *Genome Biol*. 2007;8(5):215. doi:10.1186/gb-
635 2007-8-5-215

636 16. van der Flier A, Sonnenberg A. Function and interactions of integrins. *Cell Tissue Res*.
637 2001;305(3):285-298. doi:10.1007/s004410100417

638 17. Walker CJ, Crocini C, Ramirez D, et al. Nuclear mechanosensing drives chromatin
639 remodelling in persistently activated fibroblasts. *Nat Biomed Eng*. 2021;5(12):1485-1499.
640 doi:10.1038/s41551-021-00709-w

641 18. Walker CJ, Batan D, Bishop CT, et al. Extracellular matrix stiffness controls cardiac
642 valve myofibroblast activation through epigenetic remodeling. *Bioeng Transl Med*.
643 2022;7(3):e10394. doi:10.1002/btm2.10394

644 19. Walker CJ, Schroeder ME, Aguado BA, Anseth KS, Leinwand LA. Matters of the heart:
645 Cellular sex differences. *J Mol Cell Cardiol*. 2021;160:42-55.
646 doi:10.1016/j.yjmcc.2021.04.010

647 20. Hartman RJG, Huisman SE, den Ruijter HM. Sex differences in cardiovascular
648 epigenetics—a systematic review. *Biol Sex Differ*. 2018;9(1):19. doi:10.1186/s13293-018-
649 0180-z

650 21. Deegan DF, Nigam P, Engel N. Sexual Dimorphism of the Heart: Genetics, Epigenetics,
651 and Development. *Front Cardiovasc Med*. 2021;8. doi:10.3389/fcvm.2021.668252

652 22. Wijchers PJ, Festenstein RJ. Epigenetic regulation of autosomal gene expression by sex
653 chromosomes. *Trends Genet*. 2011;27(4):132-140. doi:10.1016/j.tig.2011.01.004

654 23. Dobson LE, Fairbairn TA, Plein S, Greenwood JP. Sex Differences in Aortic Stenosis and
655 Outcome Following Surgical and Transcatheter Aortic Valve Replacement. *J Womens Health*.
656 2015;24(12):986-995. doi:10.1089/jwh.2014.5158

657 24. Côté N, Clavel MA. Sex Differences in the Pathophysiology, Diagnosis, and
658 Management of Aortic Stenosis. *Cardiol Clin*. 2020;38(1):129-138.
659 doi:10.1016/j.ccl.2019.09.008

660 25. Fleury MA, Annabi MS, Voisine M, et al. Impact of sex and sex hormones on
661 pathophysiology and progression of aortic stenosis in a murine model. *Physiol Rep*. 2022;
662 10(16): e15433. doi: 10.14814/phy2.15433

663 26. Aguado BA, Walker CJ, Grim JC, et al. Genes That Escape X Chromosome Inactivation
664 Modulate Sex Differences in Valve Myofibroblasts. *Circulation*. 2022;145(7):513-530.
665 doi:10.1161/CIRCULATIONAHA.121.054108

666 27. Vogt BJ, Peters DK, Anseth KS, Aguado BA. Inflammatory serum factors from aortic
667 valve stenosis patients modulate sex differences in valvular myofibroblast activation and
668 osteoblast-like differentiation. *Biomater Sci*. 2022;10(22):6341-6353.
669 doi:10.1039/D2BM00844K

670 28. James BD, Allen JB. Sex-Specific Response to Combinations of Shear Stress and
671 Substrate Stiffness by Endothelial Cells In Vitro. *Adv Healthc Mater*. 2021;10(18):2100735.
672 doi:10.1002/adhm.202100735

673 29. Sánchez Marrero G, Villa-Roel N, Li F, et al. Single-Cell RNA sequencing investigation
674 of female-male differences under PAD conditions. *Front Cardiovasc Med*. 2023;10.
675 doi:10.3389/fcvm.2023.1251141

676 30. Mas-Peiro S, Abplanalp WT, Rasper T, et al. Mosaic loss of Y chromosome in monocytes
677 is associated with lower survival after transcatheter aortic valve replacement. *Eur Heart J*.
678 2023;44(21):1943-1952. doi:10.1093/eurheartj/ehad093

679 31. Sano S, Horitani K, Ogawa H, et al. Hematopoietic loss of Y chromosome leads to
680 cardiac fibrosis and heart failure mortality. *Science*. 2022;377(6603):292-297.
681 doi:10.1126/science.abn3100

682 32. Thompson DJ, Genovese G, Halvardson J, et al. Genetic predisposition to mosaic Y
683 chromosome loss in blood. *Nature*. 2019;575(7784):652-657. doi:10.1038/s41586-019-1765-3

684 33. Y-Chromosome Gene, Uty, Protects Against Pulmonary Hypertension by Reducing
685 Proinflammatory Chemokines | American Journal of Respiratory and Critical Care Medicine.
686 Accessed May 13, 2024. https://www.atsjournals.org/doi/full/10.1164/rccm.202110-2309OC

687 34. Puperi DS, Balaoing LR, O'Connell RW, West JL, Grande-Allen KJ. 3-Dimensional
688 spatially organized PEG-based hydrogels for an aortic valve co-culture model. *Biomaterials*.
689 2015;67:354-364. doi:10.1016/j.biomaterials.2015.07.039

690 35. Puperi DS, Kishan A, Punske ZE, et al. Electrospun Polyurethane and Hydrogel
691 Composite Scaffolds as Biomechanical Mimics for Aortic Valve Tissue Engineering. *ACS*
692 *Biomater Sci Eng*. 2016;2(9):1546-1558. doi:10.1021/acsbiomaterials.6b00309

693 36. Porras AM, Westlund JA, Evans AD, Masters KS. Creation of disease-inspired
694 biomaterial environments to mimic pathological events in early calcific aortic valve disease.
695 *Proc Natl Acad Sci*. 2018;115(3):E363-E371. doi:10.1073/pnas.1704637115

696 37. Scott AJ, Simon LR, Hutson HN, Porras AM, Masters KS. Engineering the aortic valve
697 extracellular matrix through stages of development, aging, and disease. *J Mol Cell Cardiol*.
698 2021;161:1-8. doi:10.1016/j.yjmcc.2021.07.009

699 38. Floy ME, Shabnam F, Givens SE, et al. Identifying molecular and functional similarities
700 and differences between human primary cardiac valve interstitial cells and ventricular
701 fibroblasts. *Front Bioeng Biotechnol*. 2023;11. Accessed July 2, 2023.
702 https://www.frontiersin.org/articles/10.3389/fbioe.2023.1102487

703 39. Driscoll K, Cruz AD, Butcher JT. Inflammatory and Biomechanical Drivers of
704 Endothelial-Interstitial Interactions in Calcific Aortic Valve Disease. *Circ Res*.
705 2021;128(9):1344-1370. doi:10.1161/CIRCRESAHA.121.318011

706 40. Grim JC, Aguado BA, Vogt BJ, et. al. Secreted Factors From Proinflammatory
707 Macrophages Promote an Osteoblast-Like Phenotype in Valvular Interstitial Cells.
708 *Arterioscler. Thromb. Vasc. Biol*. 2020; ;40(11):e296-e308. doi:
709 10.1161/ATVBAHA.120.315261

710 41. Chen G, Deng C, Li YP. TGF-β and BMP Signaling in Osteoblast Differentiation and
711 Bone Formation. *Int J Biol Sci*. 2012;8(2):272-288. doi:10.7150/ijbs.2929

712 42. Vander Ark A, Cao J, Li X. TGF-β receptors: In and beyond TGF-β signaling. *Cell*
713 *Signal*. 2018;52:112-120. doi:10.1016/j.cellsig.2018.09.002

714 43. Yang P, Troncone L, Augur ZM, Kim SSJ, McNeil ME, Yu PB. The role of bone
715 morphogenetic protein signaling in vascular calcification. *Bone*. 2020;141:115542.
716 doi:10.1016/j.bone.2020.115542

717 44. Zhang J, Chen Y, Gao M, et. al. Silver Nanoparticles Compromise Female Embryonic
718 Stem Cell Differentiation through Disturbing X Chromosome Inactivation. *ACS Nano*. 2019;
719 13, 2, 2050–2061. doi:10.1021/acsnano.8b08604

720 45. Richards JM, Kunitake JAMR, Hunt HB, et al. Crystallinity of hydroxyapatite drives
721 myofibroblastic activation and calcification in aortic valves. *Acta Biomater*. 2018;71:24-36.
722 doi:10.1016/j.actbio.2018.02.024

723 46. Félix Vélez NE, Gorashi RM, and Aguado BA. Chemical and molecular tools to probe
724 biological sex differences at multiple length scales. J. Mater. Chem. B. 2022;10, 7089-7098.
725 doi: 10.1039/D2TB00871H

726 47. Fogg K, Tseng NH, Peyton SR, et. al. Roadmap on biomaterials for women's health. J.
727 Phys. Mater. 2023;6 012501. doi: 10.1088/2515-7639/ac90ee
728

729 48. Aguado BA, Schuetze KB, Grim JC, et al. Transcatheter aortic valve replacements alter
730 circulating serum factors to mediate myofibroblast deactivation. Sci Trans Med,
731 2019;11(509):eaav3233. doi: 10.1126/scitranslmed.aav3233
732
733
734
735

Figure 1

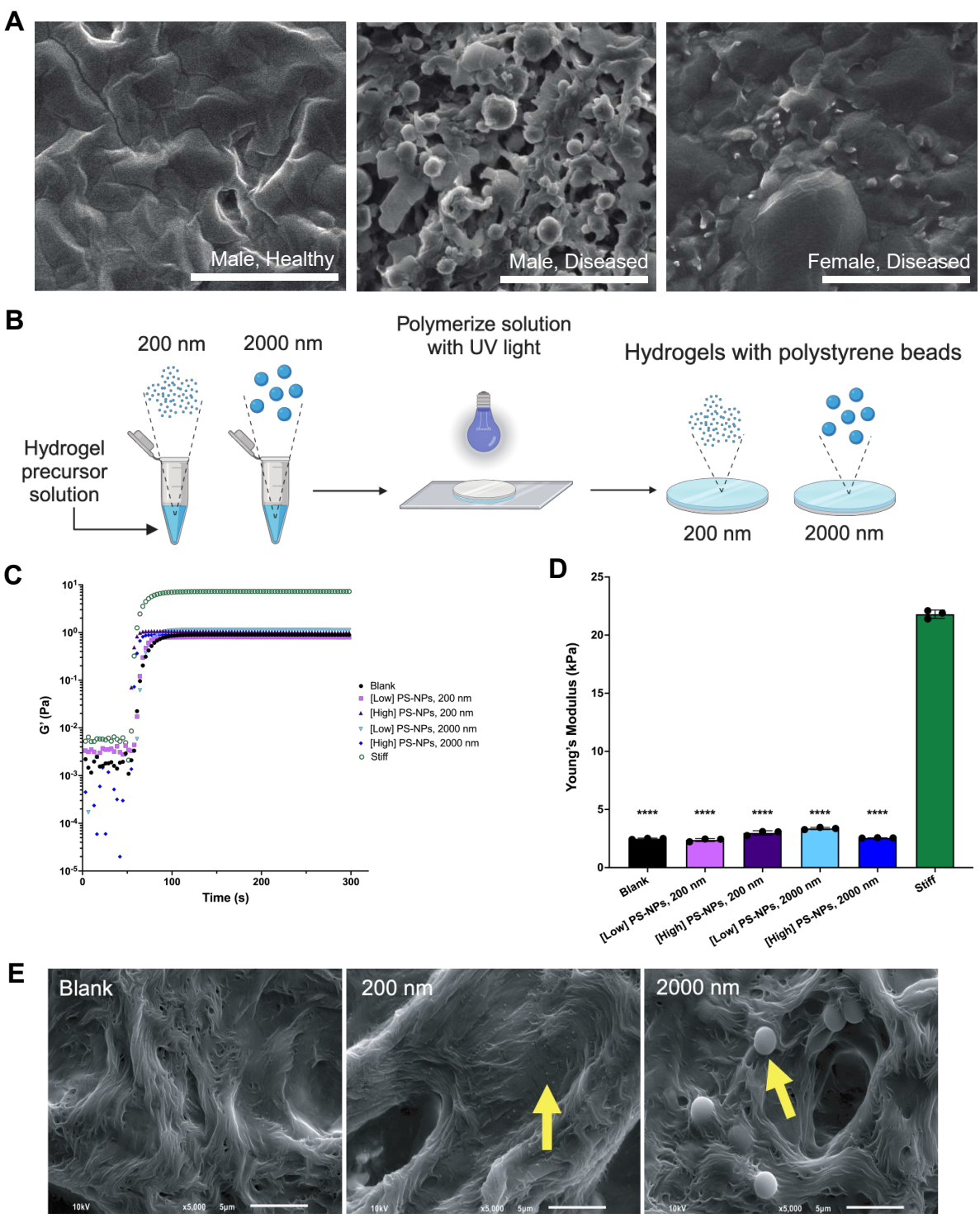
A
Male, Healthy
Male, Diseased
Female, Diseased
B
200 nm
2000 nm
Polymerize solution with UV light
Hydrogels with polystyrene beads
Hydrogel precursor solution
200 nm
2000 nm
C
G' (Pa)
Time (s)
Blank
[Low] PS-NPs, 200 nm
[High] PS-NPs, 200 nm
[Low] PS-NPs, 2000 nm
[High] PS-NPs, 2000 nm
Stiff
D
Young's Modulus (kPa)
Blank
[Low] PS-NPs, 200 nm
[High] PS-NPs, 200 nm
[Low] PS-NPs, 2000 nm
[High] PS-NPs, 2000 nm
Stiff
E
Blank
200 nm
2000 nm

759 **Figure 2**

760

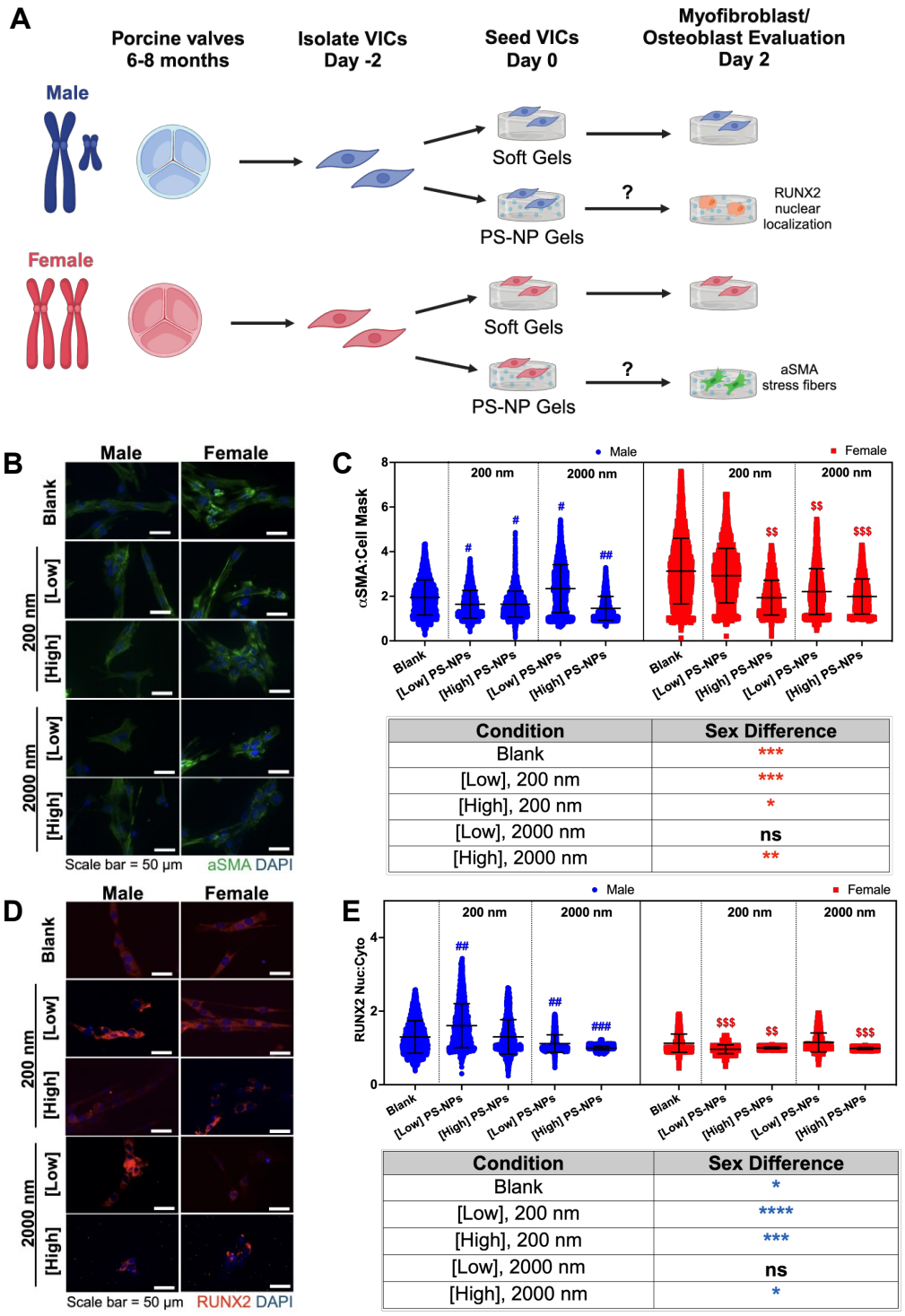

Condition	Sex Difference
Blank	***
[Low], 200 nm	***
[High], 200 nm	*
[Low], 2000 nm	ns
[High], 2000 nm	**

Condition	Sex Difference
Blank	*
[Low], 200 nm	****
[High], 200 nm	***
[Low], 2000 nm	ns
[High], 2000 nm	*

781

Figure 3

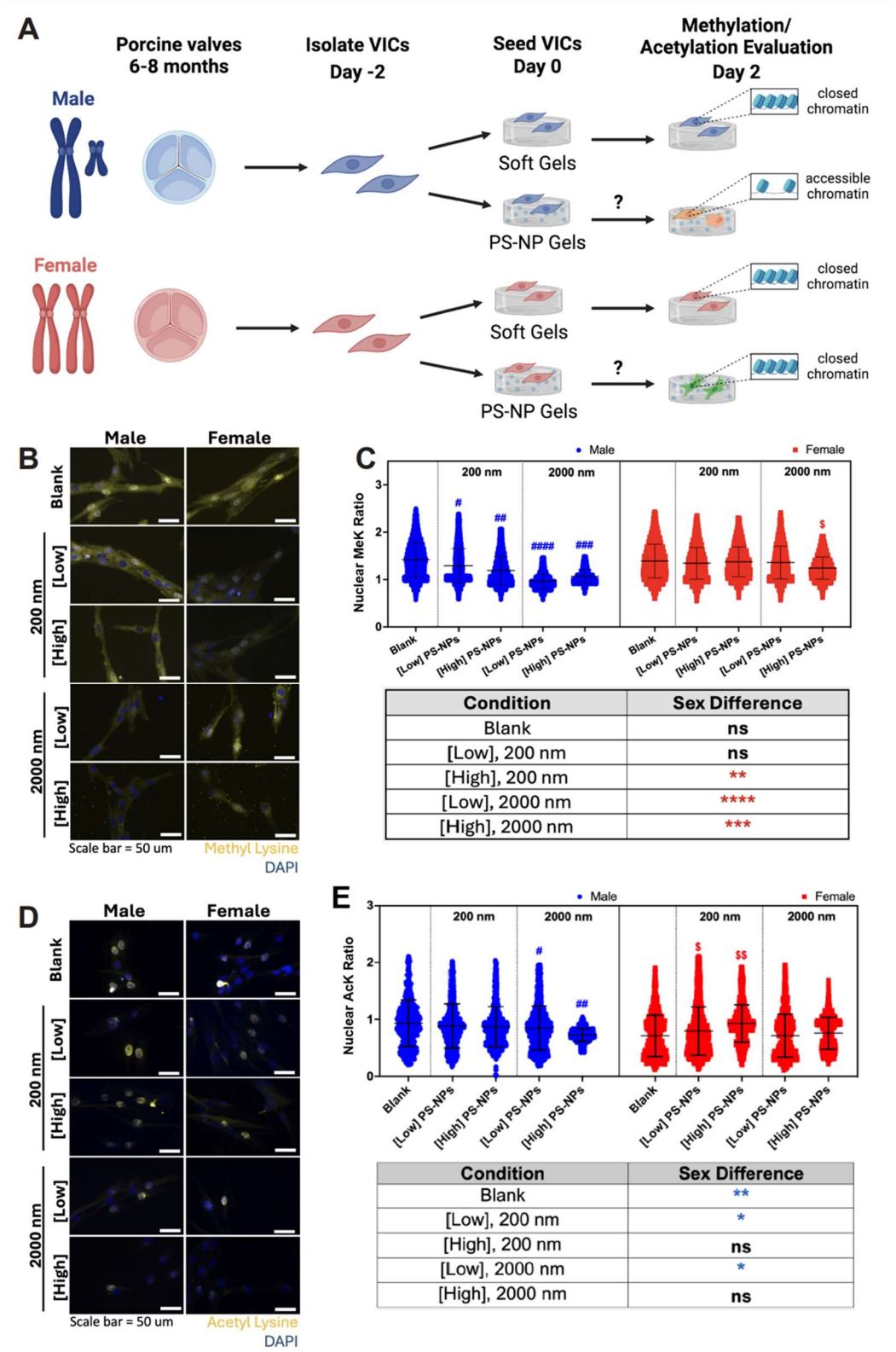

Condition	Sex Difference
Blank	ns
[Low], 200 nm	ns
[High], 200 nm	**
[Low], 2000 nm	****
[High], 2000 nm	***

Condition	Sex Difference
Blank	**
[Low], 200 nm	*
[High], 200 nm	ns
[Low], 2000 nm	*
[High], 2000 nm	ns

Figure 4

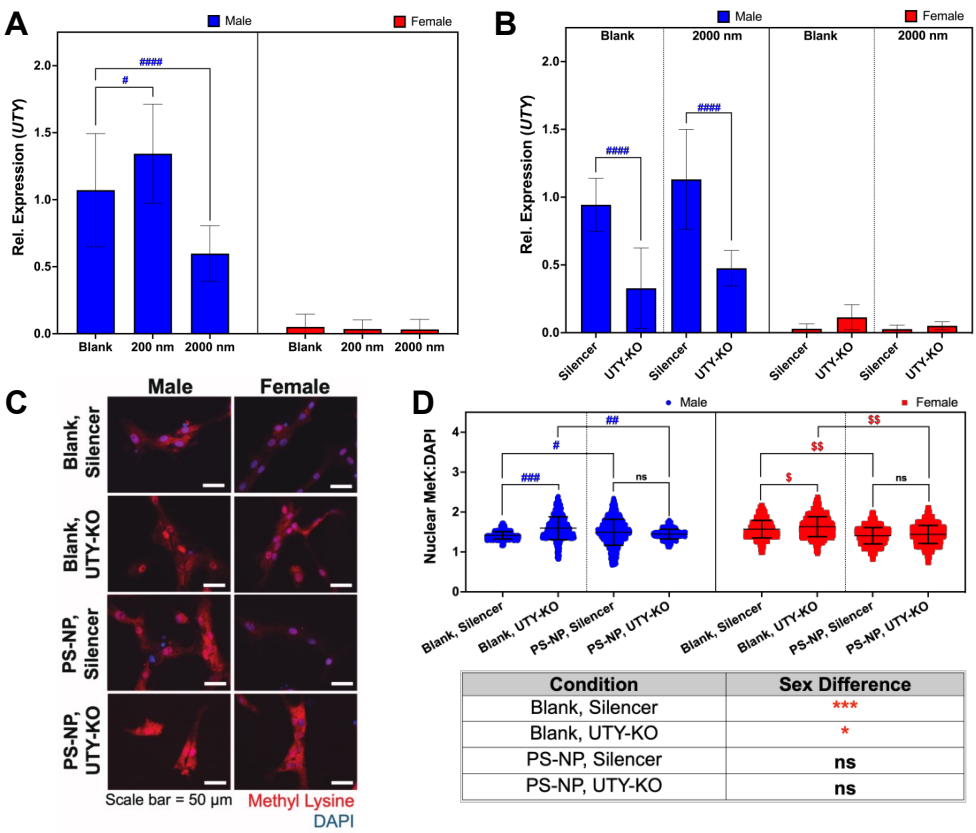

Condition	Sex Difference
Blank, Silencer	***
Blank, UTY-KO	*
PS-NP, Silencer	ns
PS-NP, UTY-KO	ns

Figure 5

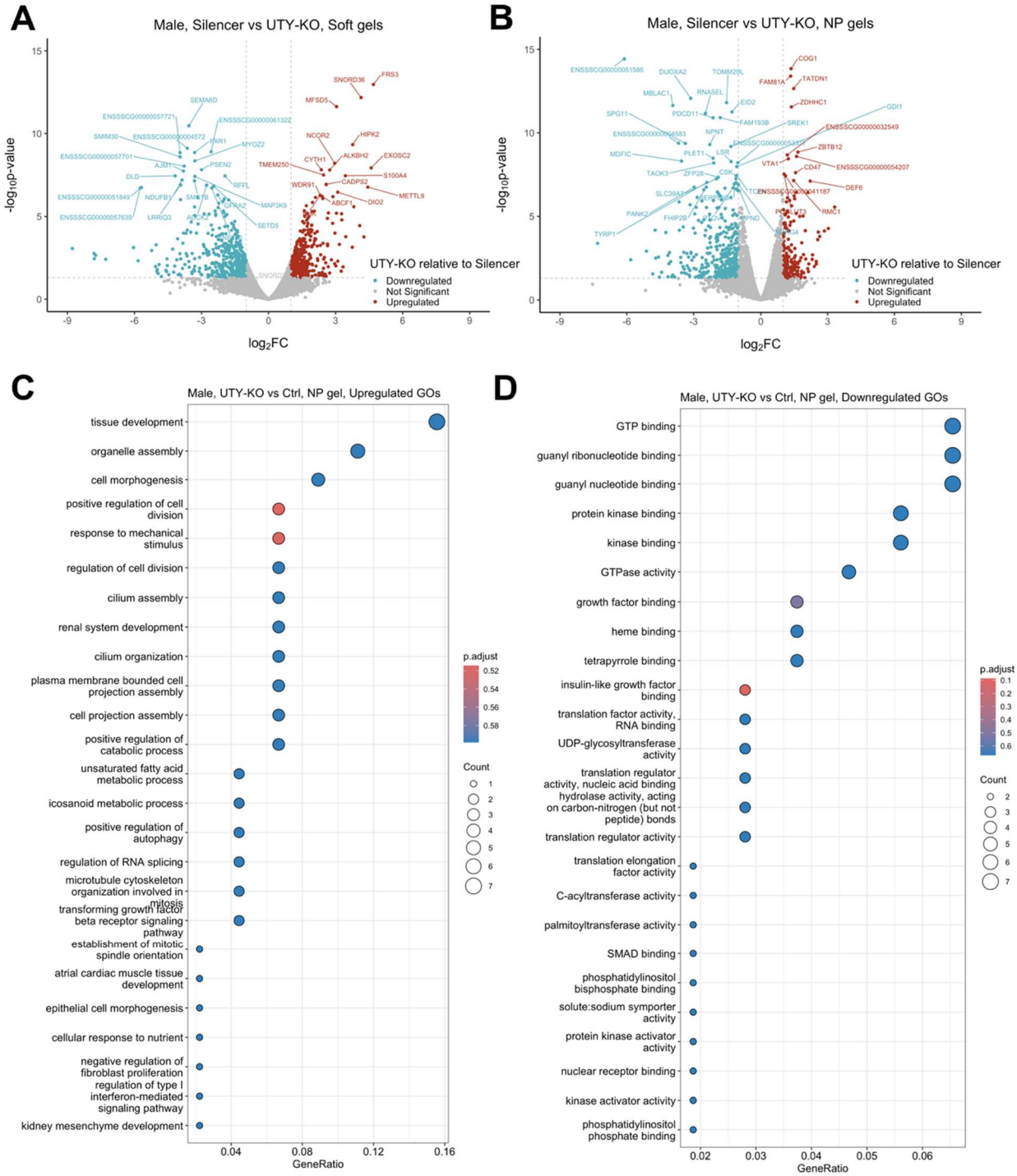
A
Male, Silencer vs UTY-KO, Soft gels
-log10p-value
log2FC
UTY-KO relative to Silencer
Downregulated
Not Significant
Upregulated
B
Male, Silencer vs UTY-KO, NP gels
-log10p-value
log2FC
UTY-KO relative to Silencer
Downregulated
Not Significant
Upregulated
C
Male, UTY-KO vs Ctrl, NP gel, Upregulated GOs
tissue development
organelle assembly
cell morphogenesis
positive regulation of cell division
response to mechanical stimulus
regulation of cell division
cilium assembly
renal system development
cilium organization
plasma membrane bounded cell projection assembly
cell projection assembly
positive regulation of catabolic process
unsaturated fatty acid metabolic process
icosanoid metabolic process
positive regulation of autophagy
regulation of RNA splicing
microtubule cytoskeleton organization involved in mitosis
transforming growth factor beta receptor signaling pathway
establishment of mitotic spindle orientation
atrial cardiac muscle tissue development
epithelial cell morphogenesis
cellular response to nutrient
negative regulation of fibroblast proliferation
regulation of type I interferon-mediated signaling pathway
kidney mesenchyme development
GeneRatio
p.adjust
Count
D
Male, UTY-KO vs Ctrl, NP gel, Downregulated GOs
GTP binding
guanyl ribonucleotide binding
guanyl nucleotide binding
protein kinase binding
kinase binding
GTPase activity
growth factor binding
heme binding
tetrapyrrole binding
insulin-like growth factor binding
translation factor activity, RNA binding
UDP-glycosyltransferase activity
translation regulator activity, nucleic acid binding
hydrolase activity, acting on carbon-nitrogen (but not peptide) bonds
translation regulator activity
translation elongation factor activity
C-acyltransferase activity
palmitoyltransferase activity
SMAD binding
phosphatidylinositol bisphosphate binding
solute:sodium symporter activity
protein kinase activator activity
nuclear receptor binding
kinase activator activity
phosphatidylinositol phosphate binding
GeneRatio
p.adjust
Count

851 **Figure 6**

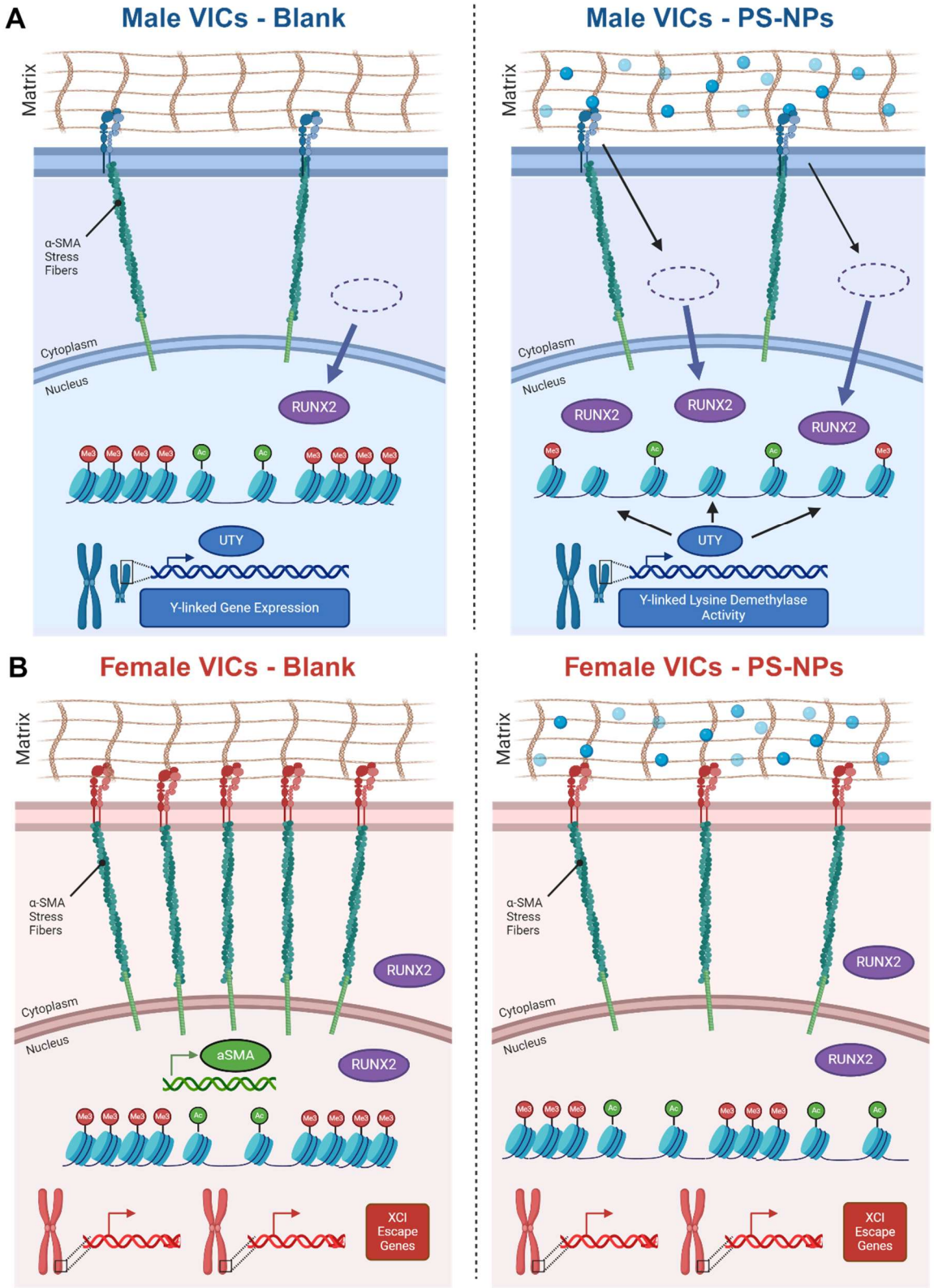

852